Superconducting nanowire single-photon detectors fabricated from atomic-layer-deposited NbN

Cite as: Appl. Phys. Lett. 115, 241101 (2019); https://doi.org/10.1063/1.5131664 Submitted: 14 October 2019 . Accepted: 26 November 2019 . Published Online: 09 December 2019

Risheng Cheng 🗓, Sihao Wang, and Hong X. Tang 🗓







ARTICLES YOU MAY BE INTERESTED IN

Deep learning optimized single-pixel LiDAR

Applied Physics Letters 115, 231101 (2019); https://doi.org/10.1063/1.5128621

Lithium-niobate-on-insulator waveguide-integrated superconducting nanowire single-photon detectors

Applied Physics Letters 116, 151102 (2020); https://doi.org/10.1063/1.5142852

NbTiN thin films for superconducting photon detectors on photonic and two-dimensional materials

Applied Physics Letters 116, 171101 (2020); https://doi.org/10.1063/1.5143986



Your Qubits. Measured.

Meet the next generation of quantum analyzers

- Readout for up to 64 qubits
 Operation at up to 8.5 GHz
 - Operation at up to 8.5 GHz, mixer-calibration-free
- Signal optimization with minimal latency



Find out more



Superconducting nanowire single-photon detectors fabricated from atomic-layer-deposited **NbN**

Cite as: Appl. Phys. Lett. 115, 241101 (2019); doi: 10.1063/1.5131664 Submitted: 14 October 2019 · Accepted: 26 November 2019 · Published Online: 9 December 2019







Risheng Cheng, (D) Sihao Wang, and Hong X. Tang^{a)} (D)



AFFILIATIONS

Department of Electrical Engineering, Yale University, New Haven, Connecticut 06511, USA

a) Electronic mail: hong.tang@yale.edu

ABSTRACT

High-quality ultrathin films of niobium nitride (NbN) are developed by the plasma-enhanced atomic layer deposition (PEALD) technique. Superconducting nanowire single-photon detectors patterned from this material exhibit high switching currents and saturated internal efficiencies over a broad bias range at a telecommunication wavelength of 1550 nm. Statistical analyses on hundreds of fabricated devices show a near-unity throughput yield due to the exceptional homogeneity of the films. The ALD-NbN material represents an ideal superconducting material for fabricating large single-photon detector arrays combining high efficiency, low jitter, and low dark counts.

Published under license by AIP Publishing. https://doi.org/10.1063/1.5131664

Superconducting nanowire single-photon detectors (SNSPDs)^{1,2} have gained widespread attention due to their excellent performances, including high efficiency,³⁻⁶ fast speed,^{7,8} exceptional timing jitter,⁹⁻ and ultralow dark count rates. 12,13 In addition, their suitability for onchip integration with various nanophotonics circuits 14-23 as well as their photon number resolving^{24–26} and spectral²⁷ resolving capability renders them an ideal choice for applications in quantum optics, quantum communications, and quantum information processing.

The SNSPD is typically a narrow nanowire (20 nm-150 nm width) patterned from an ultrathin superconducting film (3-10 nm thickness) for absorbing incident photons. So far, two main classes of superconducting materials have been utilized to fabricate highefficiency SNSPDs: (1) polycrystalline nitride superconductors such as NbN^{4,15,33} and NbTiN; ^{5,16,34–36} (2) amorphous alloy superconductors, such as WSi, ^{3,37} MoSi, ^{6,11,21,38,39} and MoGe. ⁴⁰ Each of these two classes of materials has their advantages and drawbacks in photon detection. The amorphous films have a smaller superconducting energy gap and lower electron density, which tend to create larger photon-excited hot spots in the nanowires and thus result in better saturated internal efficiency. The structural homogeneity due to the absence of grain boundaries in these films further enables the fabrication of large-area detector arrays without suffering from serious constrictions. 41,42 The drawback is their relatively low superconducting transition temperature T_c (<5 K for thin films), which sets their operation temperature below 2.5 K in order to achieve saturated efficiency at a wavelength of 1550 nm. 43 Polycrystalline Nb(Ti)N-based detectors, on the other hand, have higher T_c , higher critical current, relatively improved jitter performance, and more immunity to latching at high operation speed due to their shorter hot spot relaxation time. 44-46 Consequently, Nb(Ti)N was exploited in the recent demonstration of gigahertzcounting-rate detectors^{7,8} and sub-3 ps timing jitter.⁹

In this Letter, we show our development of high-quality NbN thin films by plasma-enhanced atomic layer deposition (PEALD) and their applications in the fabrication of SNSPDs. The fabricated detectors demonstrate broad saturated plateaus in the efficiency curves that are comparable with amorphous detectors, while simultaneously maintaining high switching currents. Statistical measurements over hundreds of detectors show a close-to-unity throughput yield of largearea detectors, indicating the high homogeneity of our films. ALD-NbN shown here provides a scalable material platform for realizing a large array of single-photon detectors with saturated efficiency and low timing jitter.

The NbN films are prepared using an Ultratech/CNT Fiji ALD system with (tert-butylimido)-tris(diethylamido)-niobium(V) (TBTDEN) as the niobium precursor and mixed N₂/H₂ as the plasma gas. In each cycle of deposition, the substrate is first exposed to the precursor to form a monolayer of TBTDEN on the surface, which is later reduced to NbN by reacting with the plasma. Ar purging is performed prior to each plasma step to remove residual TBTDEN. By alternating these steps, the NbN film is deposited on the substrate with

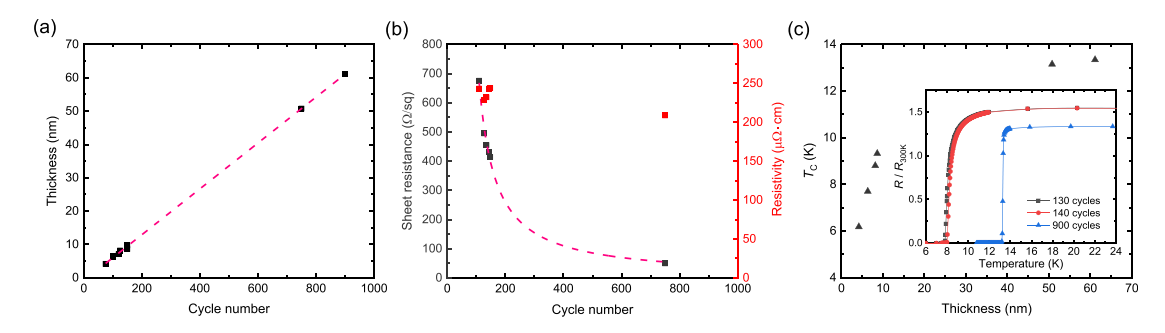


FIG. 1. (a) Measured NbN film thickness vs the ALD cycle number. The dashed line is a linear fit, whose slope indicates a deposition rate of 0.68 Å/cycle. (b) Measured sheet resistance (R_{sheet}) and calculated resistivity of the NbN films vs the ALD cycle number (x). The dashed line represents a fit by the equation $R_{\text{sheet}} = B/(x-a)$ with B and A as the free fitting parameters. (c) B0 of the NbN films vs the thickness. Inset: resistance of three NbN films vs temperature showing the superconducting transition. The resistance is normalized by the room temperature value B100 of the NbN films vs temperature value B100 o

atomic level thickness control. The best results combining the highest $T_{\rm c}$ as well as the lowest resistivity are achieved at the substrate temperature of 300 °C and the plasma power of 300 W. More details on the preparation process including other optimized parameters could be found in Ref. 47.

Figure 1(a) plots the measured NbN film thickness with respect to the number of deposition cycles. All the NbN films are deposited on thermally oxidized Si chips with 330 nm-thick LPCVD-grown SiN_x on top for future photonic circuit integration of the SNSPDs. 16,28 The thickness is measured using a spectroscopic ellipsometer (J. A. Woollam M-2000). The slope extracted from the linear fit (dashed line) indicates a deposition rate $DR = 0.68 \pm 0.01$ Å/cycle. Figure 1(b) shows the sheet resistance measured by the four probe and van der Pauw method on the unpatterned bare NbN films as a function of the cycle number. The dashed line represents a fit to the experimental data using the equation $R_{\text{sheet}} = B/(x-a)$, where R_{sheet} and x denote the sheet resistance and the cycle number, respectively. The best fitting is done by the set of free parameters $B=38\,178\,\Omega/\mathrm{sq}$ and a=52.9. The nonzero value of a suggests the existence of "dead cycles," which does not contribute to the conductance of the film. Based on the obtained DR in Fig. 1(a), we estimate the corresponding thickness to the "dead cycles" to be approximately 3.6 nm, which is significantly larger than the sputtered NbN films shown in another work. 48 The underlying mechanism is subject to further investigation. We also show in Fig. 1(b) the calculated resistivity by multiplying R_{sheet} with the effective thickness $(x-a) \times DR$. We observe a consistent resistivity of around 240 $\mu\Omega$ cm for the thin films (<10 nm thickness), which is slightly larger than 210 $\mu\Omega$ cm obtained from thicker films (>50 nm thickness).

In order to investigate the superconducting property of the NbN films, multiple NbN chips are cooled down in a physical property measurement system (Quantum Design PPMS DynaCool) to record the temperature dependence of the resistance. Figure 2(c) shows the film thickness dependence of T_c , which is defined as the temperature where the resistance of the film is dropped to 50% of R_{20K} , the resistance measured at 20 K. As expected, higher T_c is observed for the thicker film, and it tends to saturate at 13.3 K with a thickness of 61 nm (900 cycles). The inset of Fig. 2(c) shows the zoomed-in view of the resistance vs temperature curves around the superconducting transition region. The very sharp transition in the 900-cycle film with only a transition width of 0.15 K (90% to 10% of R_{20K}) suggests high homogeneity and uniformity of the deposited film. The 130-cycle and

140-cycle films that are later fabricated into nanowire detectors exhibit reduced T_c around 8 K and broader transition with a width of 1.7 K.

We fabricate SNSPDs by patterning the 130-cycle and 140-cycle NbN films deposited on SiN_x chips. We define superconducting

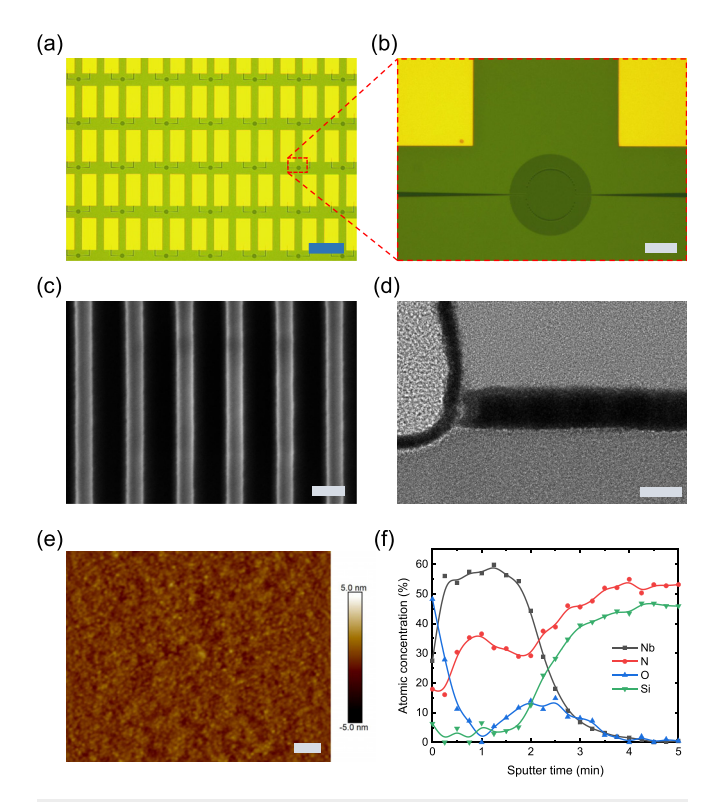


FIG. 2. (a) Optical micrograph of the fabricated SNSPD array. Scale bar: 200 μ m. (b) Close-up view of the nanowire detection area of an SNSPD. Scale bar: 10 μ m. (c) Close-up SEM image of an SNSPD with 50 nm-width nanowires. The pitch of the nanowires is kept three times the width. Scale bar: 100 nm. (d) TEM image taken at the edge of the nanowire cross section patterned from the 140-cycle NbN film. The HSQ mask is left on top after the fabrication. Scale bar: 10 nm. (e) AFM image taken on the bare 140-cycle NbN film prior to the device patterning. Scale bar: 100 nm. (f) XPS measurement results of the 140-cycle NbN film showing the depth profile of the atomic concentration for multiple concerned elements.

nanowires by the exposure to a negative-tone 6% hydrogen silsesquioxane (HSQ) resist using high-resolution (100 kV) electron-beam lithography (Raith EBPG5200) and the subsequent development in tetramethylammonium hydroxide (TMAH)-based developer MF-312. In a second electron-beam lithography step, contact electrodes are defined using double-layer polymethyl methacrylate (PMMA) positive-tone resist. After the development in the mixture of methyl isobutyl ketone (MIBK) and isopropyl alcohol (IPA), we liftoff the electron-beam evaporated 10 nm-thick Cr adhesion layer and 100 nmthick Au in acetone to form the contact pads. Later, the HSQ nanowire pattern is transferred to the NbN layer in a timed reactive-ion etching (RIE) step employing tetrafluoromethane (CF₄) chemistry.

On each NbN chip, we fabricate a total of 450 SNSPDs with three different designs that employ nanowires of nominal widths 50 nm, 75 nm, and 100 nm, respectively [Fig. 2(a)]. As shown in Fig. 2(b), the nanowires are meandered into a circular shape of diameter 15 μm to form the active detection area, while the pitch of the nanowires is kept three times the width. The extra floating nanowires surrounding the active area are for proximity effect correction during the electronbeam exposure, which constitute a larger circle of diameter $25 \,\mu m$ along with the active area. Figure 2(c) shows the scanning electron micrograph (SEM) image for one of the 50 nm-width devices. The fabricated nanowires demonstrate high uniformity with less than 5 nm width variation across the whole active area of the device. In the meantime, the uniformity of the long nanowires is also guaranteed by the ultrasmooth surface of the NbN film. As visualized in Fig. 2(e), the atomic force micrograph (AFM) image taken on the NbN film prior to the device patterning demonstrates a better than 0.4 nm root mean square surface roughness with a negligible difference from the original SiN_x substrate.

Figure 2(d) presents the transmission electron micrograph (TEM) image taken at the edge of the nanowire cross section with the HSQ mask left on top. The total thickness of the nanowire (patterned from 140-cycle NbN film) is approximately 9.5 nm including the 2 nm-thick native oxide layer, which could be distinguished from the slight color difference. For further investigation of the elemental composition, we perform X-ray photoelectron spectroscopy (XPS) measurement on the unpatterned NbN film. By slowly sputtering the target film using a focused Ar ion beam, the depth profile of the atomic concentration for multiple concerned elements could be obtained. As shown in Fig. 2(f), the existence of the native oxide layer is further confirmed by the high concentration of oxygen observed during the first 0.5 min sputtering, which decays rapidly as the element analysis is performed deeper into the film. Notably, we observe another oxygen peak at the interface between NbN and the SiNx substrate. The existence of this initial layer of oxide leads to a change in the property of NbN films and could be the origin of the aforementioned "dead cycles." A separate XPS measurement is also carried out on the thicker 900-cycle NbN film after 6 min Ar sputtering to completely remove the surface oxide layer and any potential contamination of the film. The element analysis results indicate 60%-65% concentration of Nb and 35%-40% N with the negligible presence of other elements.

The detector chips are mounted on a 3-axis stack of Attocube stages inside a closed-cycle refrigerator and cooled down to 1.7 K base temperature. In order to characterize the optical response of the fabricated detectors, 1550 nm continuous wave (CW) laser light is attenuated to the single-photon level and sent to the detector chips via a

standard telecommunication fiber (SMF-28) installed in the refrigerator. The detectors are flood-illuminated by fixing the fiber tip far away from the surface of the detector chips, and the diameter of the provided beam spot on the chip is estimated to be around 2 mm. We control the Attocube stages using the LabVIEW program to move the detector chips and make an electrical contact between the RF probes and the gold pads of the detectors. The RF probes are connected to a coaxial cable installed in the refrigerator, and the room-temperature end of the cable is attached to a bias-tee (Mini-Circuits ZFBT-6GW+) to separate the DC bias current and RF output pulses for the detectors. The output pulses are amplified by a low-noise RF amplifier (RF bay LNA-650) and sent to a fast oscilloscope for pulse observation or a pulse counter (PicoQuant PicoHarp 300) for the photon counting measurement.

All the detectors are screened using an automated measurement program, and several best detectors with the highest switching currents I_{SW} are selected for subsequent more detailed optical characterization. Figure 3 plots the normalized photon counts as a function of the relative bias current ($I_{\rm bias}/I_{\rm SW}$) for SNSPDs of different widths and thicknesses. The I_{SW} values of the 100 nm, 75 nm, and 50 nm-width nanowires patterned from the 140-cycle (130-cycle) NbN film are $21.9 \,\mu\text{A} \, (17.6 \,\mu\text{A}), \, 16.3 \,\mu\text{A} \, (12.4 \,\mu\text{A}), \, \text{and} \, \, 11.1 \,\mu\text{A} \, (6.9 \,\mu\text{A}), \, \text{respec-}$ tively. All the measured detectors demonstrate very broad saturated response plateaus, indicating high internal efficiencies of the detectors. The broad plateaus not only render the detectors less sensitive to the constriction but also enable the operation of the detectors in a lower bias region with much lower intrinsic dark counts and without compromising the high efficiency. It is worth noting that the broad plateaus shown here are comparable with the amorphous detectors, while the high $I_{\rm SW}$ is not compromised. Our 100 nm-width detectors made from the 140-cycle NbN film still demonstrate a well-saturated efficiency with a significantly improved I_{SW} larger than 20 μ A. This feature eases the fabrication process and also promises faster detectors with low timing jitter.

The high homogeneity of our NbN films could also be seen in the I_{SW} histogram for the detectors of different designs visualized in

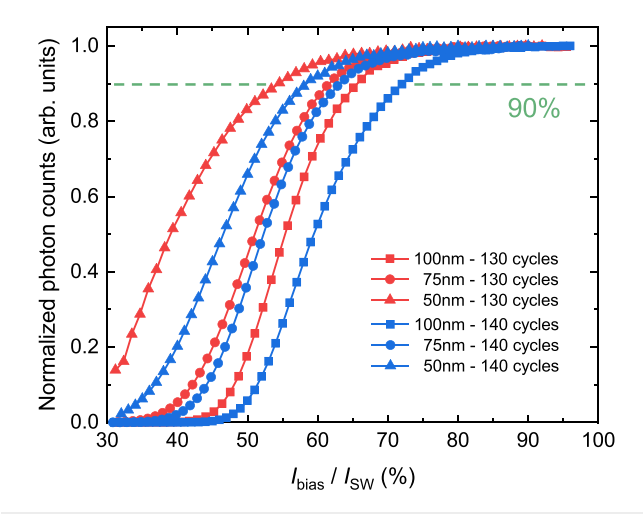


FIG. 3. Normalized photon counts vs the relative bias current $(l_{\rm bias}/l_{\rm SW})$ for SNSPDs of varying width and thickness. The saturation current $l_{\rm sat}$ is defined as the current where 90% of the maximum counting rate is reached.

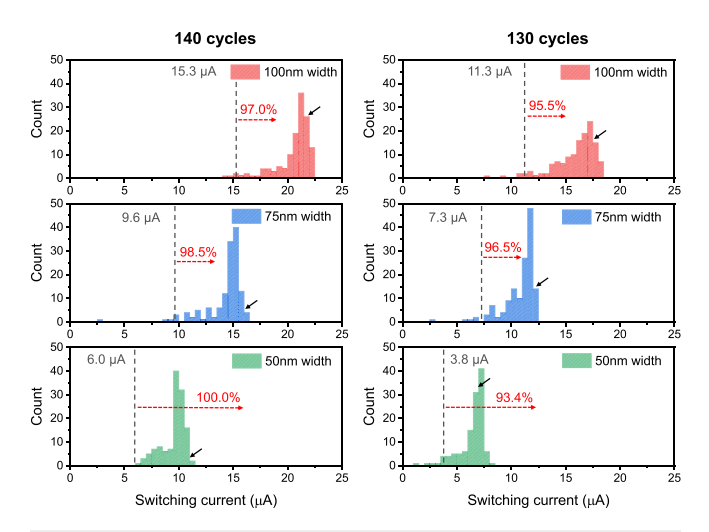


FIG. 4. Histogram of I_{SW} measured from SNSPDs of varying width and thickness. The gray dashed lines represent I_{sat} for each type of devices, and the calculated throughput yields are shown by the red dashed arrows. $I_{\rm SW}$ of the reference detectors shown in Fig. 3 are marked using the black solid arrows.

Fig. 4. The results show a highly concentrated distribution of I_{SW} , except for just a small number of nanowires showing reduced I_{SW} possibly due to the constriction. Since it is extremely time-consuming to perform the optical characterization for all the detectors, we compare I_{SW} with the reference detectors of the same design shown in Fig. 3 for the estimation of the detector throughput yield. For each type of detector, we first define a saturation current I_{sat} as the current where 90% of the maximum counting rates are reached (see green dashed lines in Fig. 3 and gray dashed lines in Fig. 4). The throughput yield is then calculated as the ratio of the number of the detectors showing I_{SW} $> I_{\rm sat}$ to the total number. Despite the large areas of the detectors, throughput yields exceeding 93% are recorded for all types of detectors. In particular, a 100% yield is demonstrated with 50 nm-width detectors patterned from the 140-cycle NbN film due to the broader saturation plateau with narrower width and also better uniformity in thickness compared to the slightly thinner 130-cycle film.

In conclusion, based on the PEALD technique, we have prepared high quality and uniform NbN films with a T_c value of up to 13.3 K and atomic level thickness control. The SNSPDs made from this material simultaneously demonstrate broad saturated efficiency plateaus and an I_{SW} value larger than 20 μ A. These features not only allow for the operation of the detectors in the lower dark count regime without compromising high efficiencies and low jitters but also render the detectors less sensitive to the constriction when fabricating large-area detector arrays. In addition, the statistical analysis on the I_{SW} histogram measured for hundreds of detectors shows a strikingly high device yield approaching unity, which we attribute to the exceptional homogeneity of the film with very few defects. We expect that the system efficiencies of our ALD-NbN detectors could be significantly improved by integrating them with optical cavities and careful alignment with optical fibers in the near future.³⁻⁶ We also envision that the ALD-NbN material will play an important role in the fabrication of integrated quantum photonic circuits where on-chip waveguideintegrated SNSPDs are in great demand.

During the preparation of this manuscript, we became aware of the work by Knehr et al. on SNSPDs fabricated from ALD-NbN.⁴

We acknowledge funding support from the DARPA DETECT program through an ARO grant (No. W911NF-16-2-0151), an NSF EFRI grant (No. EFMA-1640959), an AFOSR MURI grant (No. FA95550-15-1-0029), and the Packard Foundation. The authors would like to thank Michael Power, Sean Rinehart, Kelly Woods, Dr. Yong Sun, Dr. Min Li, Dr. Lei Wang, and Dr. Michael Rooks their assistance provided in the film deposition, characterization, and device fabrication. The characterization of the NbN films was done at the Yale West Campus Materials Characterization Core (MCC). The fabrication of the devices was done at the Yale School of Engineering & Applied Science (SEAS) Cleanroom and the Yale Institute for Nanoscience and Quantum Engineering (YINQE).

REFERENCES

- ¹C. M. Natarajan, M. G. Tanner, and R. H. Hadfield, Supercond. Sci. Technol. **25**, 063001 (2012).
- ²G. Gol'Tsman, O. Okunev, G. Chulkova, A. Lipatov, A. Semenov, K. Smirnov, B. Voronov, A. Dzardanov, C. Williams, and R. Sobolewski, Appl. Phys. Lett. 79, 705 (2001).
- ³F. Marsili, V. B. Verma, J. A. Stern, S. Harrington, A. E. Lita, T. Gerrits, I. Vayshenker, B. Baek, M. D. Shaw, R. P. Mirin et al., Nat. Photonics 7, 210
- ⁴W. Zhang, L. You, H. Li, J. Huang, C. Lv, L. Zhang, X. Liu, J. Wu, Z. Wang, and X. Xie, Sci. China Phys., Mech. Astron. 60, 120314 (2017).
- ⁵I. Esmaeil Zadeh, J. W. Los, R. B. Gourgues, V. Steinmetz, G. Bulgarini, S. M. Dobrovolskiy, V. Zwiller, and S. N. Dorenbos, APL Photonics 2, 111301 (2017).
- ⁶D. V. Reddy, R. R. Nerem, A. E. Lita, S. W. Nam, R. P. Mirin, and V. B. Verma, CLEO: QELS_Fundamental Science (Optical Society of America, 2019), p. FF1A-3.

 ⁷W. Zhang, J. Huang, C. Zhang, L. You, C. Lv, L. Zhang, H. Li, Z. Wang, and X.
- Xie, IEEE Trans. Appl. Supercond. 29, 1 (2019).
- ⁸A. Vetter, S. Ferrari, P. Rath, R. Alaee, O. Kahl, V. Kovalyuk, S. Diewald, G. N. Goltsman, A. Korneev, C. Rockstuhl et al., Nano Lett. 16, 7085 (2016).
- ⁹B. Korzh, Q. Zhao, S. Frasca, J. Allmaras, T. Autry, E. Bersin, M. Colangelo, G. Crouch, A. Dane, T. Gerrits et al., preprint arXiv:1804.06839 (2018).
- 10 I. E. Zadeh, J. W. Los, R. Gourgues, G. Bulgarini, S. M. Dobrovolskiy, V. Zwiller, and S. N. Dorenbos, preprint arXiv:1801.06574 (2018).
- ¹¹M. Caloz, B. Korzh, E. Ramirez, C. Schönenberger, R. J. Warburton, H. Zbinden, M. D. Shaw, and F. Bussières, preprint arXiv:1906.02073 (2019).
- ¹²C. Schuck, W. H. Pernice, and H. X. Tang, Sci. Rep. 3, 1893 (2013).
- 13H. Shibata, K. Shimizu, H. Takesue, and Y. Tokura, Opt. Lett. 40, 3428 (2015).
- ¹⁴J. Sprengers, A. Gaggero, D. Sahin, S. Jahanmirinejad, G. Frucci, F. Mattioli, R. Leoni, J. Beetz, M. Lermer, M. Kamp et al., Appl. Phys. Lett. 99, 181110 (2011).
- 15 W. H. Pernice, C. Schuck, O. Minaeva, M. Li, G. Goltsman, A. Sergienko, and H. Tang, Nat. Commun. 3, 1325 (2012).
- ¹⁶C. Schuck, W. Pernice, and H. Tang, Appl. Phys. Lett. **102**, 051101 (2013).
- ¹⁷D. Sahin, A. Gaggero, J.-W. Weber, I. Agafonov, M. A. Verheijen, F. Mattioli, J. Beetz, M. Kamp, S. Höfling, M. C. van de Sanden et al., IEEE J. Sel. Top. Quantum Electron. 21, 1 (2015).
- ¹⁸O. Kahl, S. Ferrari, V. Kovalyuk, G. N. Goltsman, A. Korneev, and W. H. Pernice, Sci. Rep. 5, 10941 (2015).
- ¹⁹P. Rath, O. Kahl, S. Ferrari, F. Sproll, G. Lewes-Malandrakis, D. Brink, K. Ilin, M. Siegel, C. Nebel, and W. Pernice, Light: Sci. Appl. 4, e338 (2015).
- ²⁰F. Najafi, J. Mower, N. C. Harris, F. Bellei, A. Dane, C. Lee, X. Hu, P. Kharel, F. Marsili, S. Assefa et al., Nat. Commun. 6, 5873 (2015).
- ²¹J. Li, R. A. Kirkwood, L. J. Baker, D. Bosworth, K. Erotokritou, A. Banerjee, R. M. Heath, C. M. Natarajan, Z. H. Barber, M. Sorel et al., Opt. Express 24, 13931

- ²²S. Ferrari, C. Schuck, and W. Pernice, Nanophotonics 7, 1725–1758 (2018).
- ²³ A. Gaggero, F. Martini, F. Mattioli, F. Chiarello, R. Cernansky, A. Politi, and R. Leoni, Optica 6, 823 (2019).
- ²⁴A. Divochiy, F. Marsili, D. Bitauld, A. Gaggero, R. Leoni, F. Mattioli, A. Korneev, V. Seleznev, N. Kaurova, O. Minaeva *et al.*, Nat. Photonics 2, 302 (2008).
- 25 R. Cheng, H. Yin, J. Liu, T. Li, H. Cai, Z. Xu, and W. Chen, IEEE Trans. Appl. Supercond. 23, 2200309 (2013).
- ²⁶D. Zhu, Q.-Y. Zhao, H. Choi, T.-J. Lu, A. E. Dane, D. Englund, and K. K. Berggren, Nat. Nanotechnol. 13, 596 (2018).
- ²⁷O. Kahl, S. Ferrari, V. Kovalyuk, A. Vetter, G. Lewes-Malandrakis, C. Nebel, A. Korneev, G. Goltsman, and W. Pernice, Optica 4, 557 (2017).
- ²⁸R. Cheng, C.-L. Zou, X. Guo, S. Wang, X. Han, and H. X. Tang, Nat. Commun. 10(1), 4104 (2019).
- ²⁹Y. Yun, A. Vetter, R. Stegmueller, S. Ferrari, W. H. Pernice, C. Rockstuhl, and C. Lee, preprint arXiv:1908.01681 (2019).
- 30 H. Takesue, S. W. Nam, Q. Zhang, R. H. Hadfield, T. Honjo, K. Tamaki, and Y. Yamamoto, Nat. Photonics 1, 343 (2007).
- ³¹S.-K. Liao, W.-Q. Cai, W.-Y. Liu, L. Zhang, Y. Li, J.-G. Ren, J. Yin, Q. Shen, Y. Cao, Z.-P. Li et al., Nature 549, 43 (2017).
- ³²J. Wang, S. Paesani, Y. Ding, R. Santagati, P. Skrzypczyk, A. Salavrakos, J. Tura, R. Augusiak, L. Mančinska, D. Bacco et al., Science 360, 285 (2018).
- 33D. Rosenberg, A. Kerman, R. Molnar, and E. Dauler, Opt. Express 21, 1440 (2013).
- ³⁴R. Cheng, X. Guo, X. Ma, L. Fan, K. Y. Fong, M. Poot, and H. X. Tang, Opt. Express 24, 27070 (2016).
- 35R. Cheng, M. Poot, X. Guo, L. Fan, and H. X. Tang, IEEE Trans. Appl. Supercond. 27, 1 (2017).
- 36 S. Miki, M. Yabuno, T. Yamashita, and H. Terai, Opt. Express 25, 6796 (2017).
- ³⁷B. Baek, A. E. Lita, V. Verma, and S. W. Nam, Appl. Phys. Lett. 98, 251105 (2011).

- ³⁸Y. P. Korneeva, M. Y. Mikhailov, Y. P. Pershin, N. Manova, A. Divochiy, Y. B. Vakhtomin, A. Korneev, K. Smirnov, A. Sivakov, A. Y. Devizenko *et al.*, Supercond. Sci. Technol. **27**, 095012 (2014).
- ³⁹M. Caloz, M. Perrenoud, C. Autebert, B. Korzh, M. Weiss, C. Schönenberger, R. J. Warburton, H. Zbinden, and F. Bussières, Appl. Phys. Lett. 112, 061103 (2018).
- ⁴⁰V. B. Verma, A. E. Lita, M. R. Vissers, F. Marsili, D. P. Pappas, R. P. Mirin, and S. W. Nam, Appl. Phys. Lett. **105**, 022602 (2014).
- ⁴¹J. P. Allmaras, A. Beyer, R. Briggs, F. Marsili, M. Shaw, G. Resta, J. Stern, V. Verma, R. Mirin, S. W. Nam et al., in 2017 Conference on Lasers and Electro-Optics (CLEO) (IEEE, 2017), pp. 1–2.
- ⁴²E. E. Wollman, V. B. Verma, A. E. Lita, W. H. Farr, M. D. Shaw, R. P. Mirin, and S. W. Nam, Optics Express **27**(24), 35279–35289 (2019).
- ⁴³V. B. Verma, B. Korzh, F. Bussieres, R. D. Horansky, A. E. Lita, F. Marsili, M. Shaw, H. Zbinden, R. Mirin, and S. Nam, Appl. Phys. Lett. 105, 122601 (2014).
- ⁴⁴F. Marsili, M. J. Stevens, A. Kozorezov, V. B. Verma, C. Lambert, J. A. Stern, R. D. Horansky, S. Dyer, S. Duff, D. P. Pappas et al., Phys. Rev. B 93, 094518 (2016).
- ⁴⁵S. Ferrari, V. Kovalyuk, W. Hartmann, A. Vetter, O. Kahl, C. Lee, A. Korneev, C. Rockstuhl, G. Gol'tsman, and W. Pernice, Opt. Express 25, 8739 (2017).
- ⁴⁶L. Zhang, L. You, X. Yang, J. Wu, C. Lv, Q. Guo, W. Zhang, H. Li, W. Peng, Z. Wang et al., Sci. Rep. 8, 1486 (2018).
- ⁴⁷M. J. Sowa, Y. Yemane, J. Zhang, J. C. Palmstrom, L. Ju, N. C. Strandwitz, F. B. Prinz, and J. Provine, J. Vac. Sci. Technol., A 35, 01B143 (2017).
- ⁴⁸O. Medeiros, M. Colangelo, I. Charaev, and K. K. Berggren, J. Vac. Sci. Technol., A 37, 041501 (2019).
- ⁴⁹E. Knehr, A. Kuzmin, M. Ziegler, S. Doerner, K. Ilin, M. Siegel, R. Stolz, and H. Schmidt, preprint arXiv:1906.05214 (2019).